AGU PUBLICATIONS

JGR

Journal of Geophysical Research: Planets

RESEARCH ARTICLE
10.1002/2014JE004733

**Key Points:**
- Graphite is the only candidate mineral to form a floatation crust on Mercury
- Partial melts of the Mercurian mantle were buoyant over the entire mantle depth
- Secondary crust material can originate from as deep as the core-mantle boundary

**Correspondence to:**
K. E. Vander Kaaden,
kvander@unm.edu

**Citation:**
Vander Kaaden, K. E., and F. M. McCubbin (2015), Exotic crust formation on Mercury: Consequences of a shallow, FeO-poor mantle, *J. Geophys. Res. Planets*, *120*, doi:10.1002/2014JE004733.

Received 30 SEP 2014
Accepted 14 JAN 2015
Accepted article online 18 JAN 2015

# Exotic crust formation on Mercury: Consequences of a shallow, FeO-poor mantle

**Kathleen E. Vander Kaaden[1] and Francis M. McCubbin[1]**

[1]Institute of Meteoritics, Department of Earth and Planetary Sciences, University of New Mexico, Albuquerque, New Mexico, USA

**Abstract** The range in density and compressibility of Mercurian melt compositions was determined to better understand the products of a possible Mercurian magma ocean and subsequent volcanism. Our experiments indicate that the only mineral to remain buoyant with respect to melts of the Mercurian mantle is graphite; consequently, it is the only candidate mineral to have composed a primary floatation crust during a global magma ocean. This exotic result is further supported by Mercury's volatile-rich nature and inexplicably darkened surface. Additionally, our experiments illustrate that partial melts of the Mercurian mantle that compose the secondary crust were buoyant over the entire mantle depth and could have come from as deep as the core-mantle boundary. Furthermore, Mercury could have erupted higher percentages of its partial melts compared to other terrestrial planets because magmas would not have stalled during ascent due to gravitational forces. These findings stem from the FeO-poor composition and shallow depth of Mercury's mantle, which has resulted in both low-melt density and a very limited range in melt density responsible for Mercury's primary and secondary crusts. The enigmatically darkened, yet low-FeO surface, which is observed today, can be explained by secondary volcanism and impact processes that have since mixed the primary and secondary crustal materials.

## 1. Introduction

The terrestrial planets that comprise our inner solar system, including the Moon, are all rocky bodies that have differentiated into a crust, mantle, and core. Furthermore, all of these bodies have undergone various igneous processes since their time of primary crust formation. These processes have resurfaced each of these bodies, at least in part, resulting in the production of a secondary crust. Mercury, however, exhibits evidence that it may differ from this typical structure. Since its first flyby encounter with Mercury on 14 January 2008, the MErcury Surface, Space ENvironment, GEochemistry and Ranging (MESSENGER) spacecraft has been collecting data on the structure, chemical makeup, and density of the planet among other important characteristics [*Solomon et al.*, 2001]. Recent MESSENGER-based observations have suggested that Mercury is made up of a crust, mantle, iron sulfide (FeS) layer, and core [*Hauck et al.*, 2013; *Smith et al.*, 2012]. The core of Mercury is likely dominated by iron; however, the high metal-silicate ratio of Mercury, along with the low inferred abundance of FeO (≤4 wt %) [*Nittler et al.*, 2011; *Weider et al.*, 2012] in the silicate portion of Mercury further supports it as an end-member among the terrestrial planets and as a unique case of planetary differentiation.

If present, the solid FeS layer is at the top of the liquid outer core where this component would be buoyant relative to the Fe-rich metal core beneath it [*Hauck et al.*, 2013]. The potential existence of this layer has important implications for the distribution of heat-producing elements in the planet's interior [*McCubbin et al.*, 2012], the impact on partitioning of Si and other light elements into the core [*Chabot et al.*, 2014; *Gessmann et al.*, 2001; *Javoy et al.*, 2010; *Li and Agee*, 2001; *Malavergne et al.*, 2010; *Ricolleau et al.*, 2011; *Tsuno et al.*, 2013], and the general thermal and magmatic evolution of the planet [*Hauck et al.*, 2013]. Above this possible layer is the mantle of Mercury. On Earth, the mantle extends to about ~3480 km depth (~135 GPa) [*Dziewonski and Anderson*, 1981]. The metal-silicate ratio of the Earth is similar to the other terrestrial planets, as exemplified by the similarity in the normalized mean moment of inertia ($I/mr^2$) values [*Ramsey and Blackett*, 1948]. On Mercury, the boundary between the silicate portion of the planet and this metal portion beneath it has been estimated to be approximately 4–7 GPa (420 ± 30 km) [*Hauck et al.*, 2013]. This shallow mantle depth places restrictions on the depth of origin of magmatic materials, as well as the mantle mineralogy. Another interesting feature discovered with data from the MESSENGER spacecraft is the low iron and high sulfur (both approximately 1 to

**Table 1.** Composition of the Ideal Northern Volcanic Plains (S free and alkali free) and the Starting Composition of Our Mixture in Weight Percent Determined From a Superliquidus Experiment[a]

| Run Number | Ideal Composition | NVP-1 |
|---|---|---|
| Capsule | | Graphite |
| Pressure (GPa) | | 3.0 |
| Temperature (°C) | | 1750 |
| | *Oxides* (*Wt* %) | |
| $SiO_2$ | 57.71 | 56.67 |
| $TiO_2$ | 1.35 | 1.22 |
| $Al_2O_3$ | 13.46 | 14.40 |
| $Cr_2O_3$ | 0.79 | 0. 37 |
| FeO | 5.20 | 5.16 |
| MgO | 15.20 | 14.43 |
| MnO | 0.70 | 0.68 |
| CaO | 5.59 | 5.26 |
| Total | 100.00 | 98.19 |

[a]Ideal composition calculated and normalized from XRS data in *Nittler et al.* [2011] and *Weider et al.* [2012].

4 wt %) on the surface of Mercury [*Evans et al.*, 2012; *Nittler et al.*, 2011; *Weider et al.*, 2012, 2014b]. These constraints lead to estimates of very low computed oxygen fugacity between 2.6 and 7.3 $\log_{10}$ units below the Iron-Wüstite buffer [*McCubbin et al.*, 2012; *Zolotov et al.*, 2013], which is the lowest oxygen fugacity yet estimated for the terrestrial planets, representing yet another end-member characteristic of the innermost planet.

With the recent estimates of Mercury's surface composition from the X-Ray Spectrometer (XRS) and Gamma Ray Spectrometer (GRS) on board MESSENGER, we now have our first opportunity to directly investigate the compositions of lavas on the planet, and indirectly investigate the chemical makeup of its interior, as well as its thermal and magmatic evolution [*Evans et al.*, 2012, 2014; *Nittler et al.*, 2011; *Peplowski et al.*, 2011, 2012a, 2012b, 2014; *Weider et al.*, 2012, 2014a, 2014b]. One particular region of interest on Mercury is the northern volcanic plains (NVP). The NVP are smooth plains [*Denevi et al.*, 2013] of reported volcanic origin that cover more than 6% of the surface area of Mercury [*Head et al.*, 2011]. Spanning a $4.7 \times 10^6$ km$^2$ region of Mercury, this distinct geologic unit is less cratered than surrounding areas and the largest product of flood volcanism that has been assessed from orbit by MESSENGER [*Head et al.*, 2011]. The NVP region is similar in composition to flood basalts and komatiites on Earth, as demonstrated by similar Mg/Si, Al/Si, and Ca/Si ratios [*Weider et al.*, 2012], although FeO abundances in the Mercurian lavas are substantially lower [*Weider et al.*, 2012]. Flood volcanism on Earth is generally produced by partial melting of mantle material that is erupted onto the surface of the planet. By inference, the NVP lavas are the most likely example of melt compositions derived from the Mercurian interior that can be assessed compositionally from orbit. Therefore, they represent the best candidate for experimental examination.

Knowledge of the density, compressibility, and other physical properties of magmas is required to understand the differentiation of planetary interiors, and subsequent primary and secondary crust formation. In this study, we performed sink-float experiments on a NVP melt composition (Table 1) in order to determine the density of secondary magmas from Mercury. Although there is some evidence that suggests this unit is not completely homogeneous [*Peplowski et al.*, 2012a; *Weider et al.*, 2015], the composition assessed from orbit is still broadly representative of Mercurian melts. Therefore, given that these experiments represent the first experimental investigation of a suspected Mercurian lava composition, these data will be able to provide first-order estimates of the density of melts on Mercury. The density of this melt was then compared with the density and compressibility of primitive low-FeO peridotite and komatiite melt compositions to constrain the full range of Mercurian melt densities that span from an analog for the Mercurian magma ocean liquid (Fe-free peridotite) to partial melts of the mantle (NVP lavas). The densities of these liquids were subsequently compared to densities of a number of rock-forming minerals over the pressure range of the Mercurian mantle (up to 7 GPa) to better constrain the thermal and magmatic evolution of Mercury.

## 2. Experimental Methods

Experiments were conducted using the sink-float technique [*Agee and Walker*, 1988] to generate a full compression curve for a NVP melt composition (Table 1). We have experimentally investigated a melt with substantially more FeO than is found as the global average on the surface of Mercury and by inference,

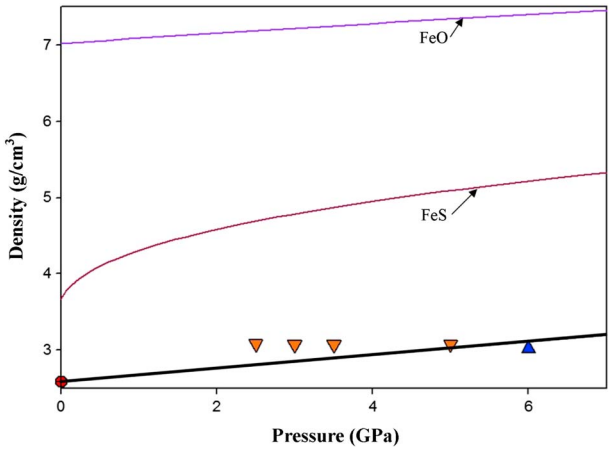


**Figure 1.** Comparison of the density of the northern volcanic plains composition with FeO and FeS melts. The maroon line is FeS melt [*Nishida et al*., 2011] and the purple line is FeO melt [*Anderson and Ahrens*, 1994]. The density of the NVP melt (same as Figures 2 and 3) is shown by the bold black line. The calculated 1 bar density (red crossed circle) for this composition at 1450°C is 2.58 g/cm$^3$ [*Lange and Carmichael*, 1987; *Ochs and Lange*, 1999]. Downward facing orange triangles represent sinking of $Fo_{100}$ spheres and the upward pointing blue triangle represents floating of $Fo_{100}$ spheres. The addition of S into our mixture would decrease the density of our melt, confirming that the volatile-free composition is an upper estimate of melt density on Mercury.

substantially higher than the bulk FeO content of the Mercurian mantle. Consequently, the melt density we report is an upper estimate for Mercurian melt compositions. Furthermore, the result of each experiment does not provide a direct measurement of the density of the liquid at the experimental conditions but rather gives an open-ended bracket on the density. Sinking spheres, referred to as a "sink," indicate that the density markers are denser than the melt, whereas floating spheres, referred to as a "float," are inferred to be less dense than the melt. However, if there is no movement of the spheres (a "neutral buoyancy"), this observation is interpreted to indicate that the density of the spheres is equivalent to that of the melt. Using this technique, the precise density of the liquid is best defined by a neutral buoyancy bracketed by a sink at slightly lower pressures and a float at slightly higher pressures. This method has been used to successfully bracket the density of silicate liquids at high pressures [*Agee and Walker*, 1993; *Agee*, 1998; *Circone and Agee*, 1996; *Knoche and Luth*, 1996; *Smith and Agee*, 1997; *Suzuki et al*., 1998; *van Kan Parker et al*., 2011; *Vander Kaaden et al*., 2015].

All experiments were conducted at the Institute of Meteoritics (IOM), University of New Mexico (UNM). A Walker-style multianvil (MA) device was used for all experiments. Density markers were crystals of well-characterized minerals with a diameter of 330–700 μm, ground to spheres using a Bond Air Mill. For all our sink-float experiments (2.5–6 GPa), forsterite-rich olivine spheres were used.

### 2.1. Starting Materials

The synthetic starting material for the northern volcanic plains melt composition was prepared at the IOM using high-purity reagent grade powdered oxides and silicates, which were mixed sequentially by volume and ground under ethanol using an automated agate mortar and pestle. All Fe in the mixtures was added as FeO in the form of synthetic fayalite. The reader is referred to *Vander Kaaden et al*. [2015] for details on the preparation of the synthetic fayalite. A superliquidus experiment was run on the synthetic composition to check that the mixture was of the appropriate bulk composition and to ensure homogeneity was maintained throughout the mixing process. The bulk composition for the synthetic melt and the targeted composition can be found in Table 1. Our NVP melt composition is free of volatile components (S, $Na_2O$, and $K_2O$) and has a higher value of FeO than reported by *Nittler et al*. [2011] and *Weider et al*. [2014b]. The volatile components have been left out of the starting material to ensure homogenization of our experimental charge under the short run conditions required for sink-float experiments (30 s). In addition, S was excluded from the experiments because S solubility is highly dependent on oxygen fugacity in silicate melts [*Berthet et al*., 2009], and it is unlikely that the experimental charge would have reached redox equilibrium and incorporate the appropriate amount of S in the silicate melt structure within the 30 s run of the sink-float experiments. The higher concentration of FeO allows us to investigate an upper limit in terms of density for Mercurian magmas. Although we excluded S, Na, and K from our starting composition, all three components would decrease the density of the NVP melt (Figure 1) [i.e. *Agee*, 2008]. Consequently, the addition of S, Na, and K, which are present in significant quantities on the Mercurian surface [*Nittler et al*., 2011; *Peplowski et al*., 2012a; *Weider et al*., 2012], would cause this melt to become less dense than reported here, so our experiments are truly exploring an upper limit melt density for the NVP lavas.

### 2.2. Sink-Float Experiments

Each experiment was set up by packing the starting material into a $Mo^0$ or graphite capsule and placing two mineral spheres, which served as density markers, at the top and bottom of the capsule. A ceramic octahedron made from Ceramcast-584 was used as the pressure medium. Rhenium foil was used as a heater, and Type C ($W_5Re_{95}/W_{26}Re_{74}$) thermocouple was located on the center of the outer surface of the heater. Two $Al_2O_3$ spacers were placed in the heater with an aluminum sheath surrounding the capsule, so it sat directly in the center of the octahedron. The octahedron was surrounded with eight tungsten carbide cubes, each with a truncation edge length of 8 mm and placed in the hatbox of the MA. The reader is referred to *Agee et al.* [1995] for pressure calibrations of our MA device.

The sample was then pressurized and rapidly heated at 200–300°C per minute to superliquidus temperatures (approximately 1700–2050°C depending on desired pressure). The experiments were held at the elevated *P-T* conditions for 30–60 s to allow the synthetic powder adequate time to melt and for the spheres to be driven up or down in the capsule by buoyancy forces. The longer run durations (60 s) were typically repeat experiments to ensure a neutral buoyancy was in fact neutral, and the lack of movement was not due to sluggish buoyancy reactions. Experiments were limited to these short run durations to prevent dissolution of the spheres into the melt, which would drive the melt composition from the target composition being investigated. The sample was quenched by shutting off the power to the furnace and allowing the run to decompress gradually. The average rate of cooling was approximately 285°C/s.

## 3. Analytical Technique

All run products were set in epoxy and then ground using sand paper with various grit sizes (53.5 μm, 36 μm, 23.6 μm, and 16 μm) until the mineral spheres were exposed. Once exposed, the samples were polished to 0.3 μm before subsequent microbeam analysis.

### 3.1. Electron Probe Microanalysis

The polished run products, including quenched materials and mineral spheres, were carbon coated and analyzed at UNM using a JEOL 8200 Electron Probe Microanalyzer (EPMA). Samples were analyzed using an accelerating voltage of 15 KeV and a beam current of 20 nA. A broad beam (10–20 μm) was used for glass analyses, whereas a focused 1 μm beam was used for the analysis of mineral density markers. The quenched melt was analyzed to determine the composition and to assess for any melt/capsule or melt/sphere interactions. The spheres were analyzed around the center to confirm composition and near the edges to ensure there was no sphere/melt interaction. Standards used for analysis include natural olivine from the Taylor standard reference block (Type 202-52; produced by the C. M. Taylor Corporation, Sunnyvale, California) for the olivine spheres, as well as almandine (analyzed for Al, Fe, and Si), augite (Si, Al, Ca, and Mg), chromite (Cr), olivine (Mg, Si, and Fe), orthoclase (Si), pyrope (Cr, Mg, Ca, and Si), titanite (Ti), and spessartine (Mn). A synthetic $CaMoO_4$ was used to determine the amount of $MoO_2$ contamination in the glasses from the capsule material for all runs. Peak and background count times were 20 s and 10 s, respectively, for major elements and 30 s and 15 s, respectively, for minor elements.

### 3.2. Micro-Fourier Transform Infrared Spectroscopy

To determine the amount of $H_2O$ in our "nominally dry" runs, two experimental charges from MA experiments on the same composition were removed from their epoxy, mounted, and doubly polished for quantitative micro-Fourier transform infrared (micro-FTIR) spectroscopic measurements. Micro-FTIR measurements were conducted on the experimental glass products at room temperature in transmittance mode with a Nicolet Nexus 670 Fourier transform infrared spectrometer in the IOM at UNM following procedures similar to *McCubbin et al.* [2008]. The interior of the IR unit was in an atmosphere purged of $H_2O$ and $CO_2$, which eliminated atmospheric absorption features. Prior to each analysis, all spots were first assessed using an optical microscope to make certain only glass was being measured during any given analysis. Transmittance IR spectra were collected over the mid-IR range (400–4000 $cm^{-1}$) from doubly polished thin sections of the run products using a Continuum microscope with a Globar source, XT-KBr beam splitter, and a mercury cadmium telluride-A detector over a 100 × 100 μm area with

**Table 2.** Equation of State Parameters for Calculating Sphere Density, Mantle Mineral Density, and Melt Density[a]

| | $K_{298}$ (GPa) | $dK/dT$ (GPa/K) | $K'$ | $\alpha_0$ (E-05) ($K^{-1}$) | $\alpha_1$ (E-09) ($K^{-1}$) | $\alpha_2$ ($K^{-1}$) | $\rho_{298}$ ($g/cm^3$) |
|---|---|---|---|---|---|---|---|
| $Mg_2SiO_4$ | 127.5[b] | −0.02[c] | 4.8[b] | 3.034 | 7.422 | −5.381E-01[d] | 3.229 $X_{Fo}$[i] |
| $Fe_2SiO_4$ | 134.6[e] | −0.024[e] | 5.2[f] | 0.2386 | 11.53 | −0.518E-01[g,h,i] | 4.417 $X_{Fa}$[i] |
| $Mg_2Al_2Si_3O_{12}$ | 171.32[j] | −0.0258[k] | 3.22[j] | 2.311 | 5.956 | −4.538E-01[l] | |
| $MgSiO_3$ | 95.8[m] | −0.0274[n] | 14.9[m] | 2.947 | 2.694 | −0.5588[K] | |
| $MgCaSi_2O_6$[o] | 110.5 | −0.0205 | 4.8 | 2.32 | 18.8 | 0 | |
| $MgAl_2O_4$[o] | 198 | −0.015 | 5.05 | 1.85 | 9.75 | −0.365 | |
| $SiO_2$[p] | 27.02 | −0.0041 | 3.8 | | | | |
| $(CaAl_2Si_2O_6)_{0.5}(NaAlSi_2O_8)_{0.5}$ | 271.85[q] | −0.0408[q] | 3.2[q] | 1.39[r] | 0.597[r] | 0[r] | |
| C (Graphite)[s] | 87.08 | | 31.52 | | | | |
| C (Diamond)[t] | 444.5 | | 4.18 | | | | |
| FeS[u] liquid | 2.5 | −0.0036 | 24 | | | | |
| FeO[v] liquid | 109.7 | −0.043 | 4.66 | | | | |

[a]Adapted from *Circone and Agee* [1996] and *van Kan Parker et al.* [2011].
[b]*Jacobs and De Jong* [2007].
[c]*Liu and Li* [2006].
[d]*Suzuki* [1975].
[e]*Graham et al.* [1988].
[f]*Isaak et al.* [1993].
[g]*Suzuki et al.* [1981].
[h]*Smyth* [1975].
[i]*Hazen* [1977].
[j]*Conrad et al.* [1999].
[k]*Sumino and Anderson* [1984].
[l]*Skinner* [1966].
[m]*Hugh-Jones and Angel* [1994]—valid up to 4 GPa.
[n]Calculated from *Hugh-Jones* [1997].
[o]*Schutt and Lesher* [2006].
[p]*Fried et al.* [2002].
[q]*Angel* [2004].
[r]*Fei* [1995].
[s]*Colonna et al.* [2011].
[t]*Dewaele et al.* [2008].
[u]*Nishida et al.* [2011].
[v]*Anderson and Ahrens* [1994].

a 4 $cm^{-1}$ resolution. Thicknesses for each sample were obtained by focusing a reflected aperture on the top surface of the sample and then the bottom surface of the sample and recording the *z* axis position of the mapping stage in the Atlus software. These arbitrary units were converted to micrometers using an empirical calibration determined specifically for our instrument [*Berger*, 2012]. Background spectra were collected under the same conditions before each analysis. Total dissolved water concentrations were determined for each glass using the calculation scheme of *Mandeville et al.* [2002] as well as the intensity of the broad OH band at 3570 $cm^{-1}$. One thousand twenty four scans were performed for each IR spectrum that we acquired.

## 4. Density Calculations

A well-defined equation of state is needed to determine the density of the spheres at the experimental pressure and temperature conditions. Additionally, in order to assess the density of this NVP melt, equation of states were used to determine the densities of many common rock-forming minerals that could be present within the Mercurian interior. The densities of the mineral markers in each experiment (olivine), as well as common rock-forming minerals, were calculated using the third-order Birch-Murnaghan equations of state [*Birch*, 1947]:

$$P = \frac{3}{2}K_T\left[\left(\frac{\rho_{T,P}}{\rho_{T,0}}\right)^{7/3} - \left(\frac{\rho_{T,P}}{\rho_{T,0}}\right)^{5/3}\right] * \left[1 - \frac{3}{4}(4 - K')\left(\left(\frac{\rho_{T,P}}{\rho_{T,0}}\right)^{2/3} - 1\right)\right] \quad (1)$$

**Table 3.** Experimental Run Conditions for Northern Volcanic Plains Sink-Float Experiments[a]

| Run Number | NVP-2 | NVP-7 | NVP-3 | NVP-4 | NVP-11 |
|---|---|---|---|---|---|
| Capsule | Graphite | Molybdenum | Graphite | Molybdenum | Molybdenum |
| Sphere | $Fo_{100}$ | $Fo_{100}$ | $Fo_{100}$ | $Fo_{100}$ | $Fo_{100}$ |
| *P* (GPa) | 2.5 | 3.0 | 3.5 | 5.0 | 6.0 |
| *T* (°C) | 1700 | 1775 | 1775 | 1950 | 2050 |
| Result | Sink | Sink | Sink | Sink | Float |
| *n* | 8 | 21 | 15 | 23 | 19 |
| $SiO_2$ | 55.85 (1.33) | 56.42 (0.45) | 55.68 (1.47) | 55.80 (0.89) | 55.95 (1.36) |
| $TiO_2$ | 1.14 (0.05) | 1.20 (0.04) | 1.14 (0.10) | 1.17 (0.05) | 1.18 (0.10) |
| $Al_2O_3$ | 14.56 (0.64) | 13.75 (0.52) | 13.41 (0.70) | 14.06 (0.93) | 12.47 (0.70) |
| $Cr_2O_3$ | 0.67 (0.05) | 0.67 (0.01) | 0.69 (0.05) | 0.71 (0.05) | 0.66 (0.02) |
| FeO | 4.83 (0.18) | 5.07 (0.07) | 4.76 (0.27) | 5.03 (0.27) | 4.93 (0.13) |
| MgO | 16.05 (1.18) | 14.93 (0.27) | 17.59 (2.39) | 16.47 (1.95) | 16.89 (0.92) |
| MnO | 0.63 (0.03) | 0.67 (0.02) | 0.63 (0.04) | 0.65 (0.05) | 0.64 (0.02) |
| CaO | 5.00 (0.15) | 4.85 (0.09) | 4.80 (0.49) | 5.06 (0.34) | 4.82 (0.16) |
| $MoO_2$ | 0.00 (0.00) | 0.52 (0.23) | 0.00 (0.02) | 1.22 (0.51) | 1.20 (1.86) |
| Total | 98.73 (0.44) | 98.07 (0.29) | 98.70 (0.40) | 100.19 (0.49) | 98.72 (0.72) |
| $\rho_{liq}$ | 2.55 | 2.54 | 2.55 | 2.54 | 2.56 |
| $\rho_{ideal\ liq}$ | 2.55 | 2.54 | 2.54 | 2.51 | 2.50 |
| $\rho_{sphere}$ | 3.05 | 3.05 | 3.04 | 3.03 | 3.00 |
| $\rho_{ideal\ 1450C}$ | 2.58 | 2.58 | 2.58 | 2.58 | 2.58 |
| $\rho_{sphere1450C}$ | 3.08 | 3.09 | 3.07 | 3.08 | 3.02 |

[a]This table gives the experimental run number, the sphere used in the experiment, the pressure (*P*) and temperature (*T*) of the experiment, the experimental sink-float result, and the number of EPMA analyses (*n*) conducted on each melt. The number in parentheses represents 1 standard deviation of the analyzed value. Also given are the average EPMA oxide compositions (wt %) and totals, the densities of the liquids from each experimental charge at the *P-T* conditions of each experiment ($\rho_{liq}$), the densities of the ideal liquids at each *P-T* ($\rho_{ideal\ liq}$), the densities of the individual spheres ($\rho_{sphere}$), and the calculated densities at 1450°C.

where $K_T$ is the isothermal bulk modulus defined as

$$K_T = K_{298} + {}^{dK}/_{dT}(T - 298) \quad (2)$$

For these equations, $K_T$ is in GPa and *T* is in Kelvin. In equation (1) *P* is pressure, *K'* is the pressure derivative, and $\rho_{T,0}$ and $\rho_{T,P}$ are the densities of the spheres at temperature *T* and ambient pressure ($10^5$ Pa) and high pressure, respectively. The density at $10^5$ Pa is given by

$$\rho_{T,0} = \rho_{298}(T) \exp \int_{298}^{T} \alpha(T) dT \quad (3)$$

in which $\alpha$ is the thermal expansion and defined as

$$\alpha(T) = \alpha_0 + \alpha_1 T + \frac{\alpha_2}{T^2} \quad (4)$$

Parameters used for each mineral are found in Table 2. The main uncertainty of the sink/float method is the calculation of sphere density through the use of these equations, which is estimated at ±0.03 g/cm$^3$ [*Circone and Agee*, 1996].

## 5. Results

### 5.1. EPMA and FTIR Results

EPMA analyses of each run product are given in Table 3. The compositions of the melts from experiment to experiment are consistent. The $Al_2O_3$ content is slightly higher than our starting material (Table 1) most likely due to slight contamination from the $Al_2O_3$ ceramic inner parts of the octahedron assembly. The higher MgO content of our final melt compositions may be the result of partial dissolution of the olivine spheres into our melt at the high temperatures of these experiments. The high $MoO_2$ analyses in NVP-4 and NVP-11 are likely due to the presence of small, unavoidable, molybdenum metal blebs interspersed through the experimental charges and do not likely reflect Mo dissolved in the silicate melt [e.g., *Burkemper et al.*, 2012].

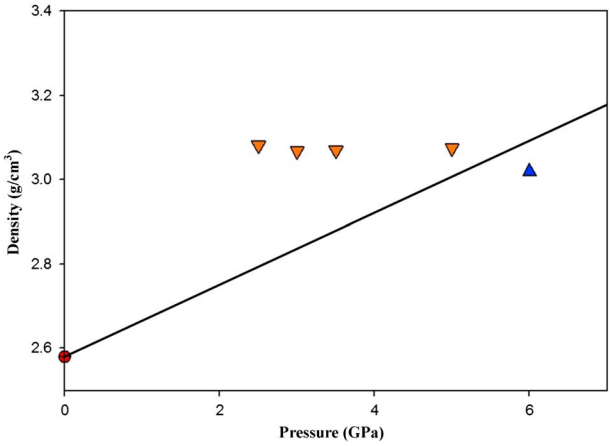


**Figure 2.** Experimental sink-float results for the NVP melt composition at $T = 1450°C$. The solid black line represents the best fit straight line to these data. Symbols are the same as in Figure 1.

Once the composition of the melts were assessed, our data were normalized to 1450°C in order to relate the density of our experiments to each other using an isothermal Birch-Murnaghan equation of state. This was done by first taking the difference between the 1 bar density of the experimental charge at the *P-T* conditions of the run ($\rho_{liq}$) and the 1 bar density of the ideal starting composition if no interactions occurred during the experiment between the melt, capsule, and density markers ($\rho_{ideal\ liq}$) at this temperature. The density of each data point was then shifted by this difference, assuming the shape of the density curve would be the same regardless of temperature (i.e., shifted either up or down). The same procedure is used to correct for compositional differences between the ideal starting composition (Table 1) and the actual composition of the melt during the run determined by EPMA. The normalized values are given in Table 3. Additionally, the two MA experiments that were used to determine the amount of $H_2O$ present in our "dry" experiments ranged in thicknesses from 48 to 120 μm. Micro-FTIR analyses of the glasses in these experiments indicate consistent water contents of ~0.3 wt % $H_2O$.

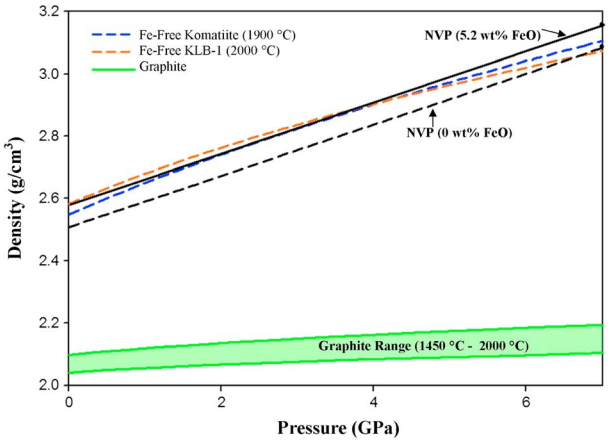


**Figure 3.** Comparison of the densities of possible Mercurian magma ocean melts. The NVP (black solid line) has been plotted using the data from Figure 2 as a maximum density end-member and removing all of the iron (black dashed line) for a minimum density end-member. Terrestrial analog melts including a FeO-free komatiite (blue dashed line) [*Agee and Walker*, 1993] and FeO-free KLB-1 peridotite (orange dashed line) [*Agee and Walker*, 1993] are shown. The FeO-free melts were plotted by calculating the 1 bar densities for the normalized FeO-free versions of each composition and constructing a parallel offset based on the density differences with the FeO-bearing compositions. All curves are plotted at their respective liquidus temperatures. The shaded region in Figure 4 was constructed using the highest and lowest densities of these lines as the outer boundaries over the given pressure range. Although we do not know an exact composition of a Mercurian magma ocean, these data show that graphite (green shaded region) will be buoyant relative to the molten bulk silicate of the Mercurian mantle. One bar densities were calculated using *Lange and Carmichael* [1987].

### 5.2. Sink-Float Results

Results from our sink-float experiments are shown in Figure 2. $Fo_{100}$ spheres sank in this melt at 2.5 GPa, 3.0 GPa, 3.5 GPa, and 5 GPa and temperatures of 1700°C, 1775°C, 1775°C, and 1950°C, respectively. These same $Fo_{100}$ spheres floated in this melt at 6 GPa and 2050°C, indicating forsterite is more dense than the Mercurian melt up to 5 GPa. A straight line has been fit to the data, instead of an equation of state, to define the maximum compressibility of this melt at 0.08 g/cm$^3$/GPa, although we acknowledge that the true compression curve is likely represented by a curved line. This line indicates that the NVP lavas are slightly more compressible than a terrestrial komatiite (0.075 g/cm$^3$/GPa) or peridotite (0.065 g/cm$^3$/GPa) melt [*Agee and Walker*, 1988, 1993], although a more realistic compression curve would essentially match terrestrial komatiite and peridotite.

## 6. Discussion

### 6.1. Range of Mercurian Melt Density

Due to the high amount of FeO and absence of light elements like Na, K, and S in our experimental starting composition,

**Table 4.** One bar Densities of Planetary Melts ($T$ at 1450°C)

| Planetary Body (Reference) | 1 Bar Density (g/cm$^3$) (Calculated From *Guo et al.* [2013], *Guo et al.* [2014], *Lange and Carmichael* [1987], *Liu and Lange* [2001], and *Ochs and Lange* [1999] | Total Range of Melt Density at 1 Bar ($\rho_{max} - \rho_{min}$) (g/cm$^3$) |
|---|---|---|
| Mercury (this study) | 2.51–2.58 | 0.07 |
| Earth (*Agee and Walker* [1993] and *Agee* [1998]) | 2.64–2.83 | 0.19 |
| Moon (*Vander Kaaden et al.* [2015]) | 2.75–3.08 | 0.33 |
| Mars (*Bertka and Fei* [1997], *Misawa* [2004], and *Warren et al.* [1996]) | 2.78–2.91 | 0.13 |

the melt density we report is an upper bound on that of Mercurian melt compositions. In an attempt to span the entire range of Mercurian melts, we have computed the density of an FeO-free end-member NVP composition to determine the lower limit of Mercurian melt density (Figure 3). Since we do not have any primitive samples of the Mercurian interior and, subsequently, do not know if the NVP composition is representative of all Mercurian melts, we have considered common terrestrial materials that may be similar to Mercurian mantle melts, including a peridotite and komatiite. However, these terrestrial liquids typically range in FeO content from ~5 to 11 wt % FeO [*Agee and Walker*, 1993], which exceeds the FeO abundances of Mercurian surface materials [*Chabot et al.*, 2014; *Charlier et al.*, 2013; *Nittler et al.*, 2011; *Weider et al.*, 2012, 2014b]. Therefore, it is more realistic to consider an FeO-free peridotite and an FeO-free komatiite as possible terrestrial analogs for Mercurian melts. As a result, the total range of Mercurian melt densities can be constrained by the density of Fe-free peridotite, Fe-free komatiite, and both Fe-bearing and Fe-free NVP lavas. This calculation was performed by first subtracting all of the iron out of the peridotite and komatiite compositions from *Agee and Walker* [1993] and renormalizing the compositions. A 1 bar density was then calculated from *Lange and Carmichael* [1987]. These FeO-free 1 bar densities, along with the bulk modulus and pressure derivative values from *Agee and Walker* [1993] for a peridotite and komatiite, respectively, were used along with the third-order Birch-Murnaghan equation of state [*Birch*, 1947] to calculate the density of each FeO-free composition. The computation of the FeO-free end-member NVP composition was conducted in a similar fashion.

These melts demonstrate a very narrow range of melt density for the silicate portion of the planet Mercury. Furthermore, the melt density is much lower than melts from other planetary bodies (Table 4) [*Agee and Walker*, 1993; *Agee*, 1998; *Bertka and Fei*, 1997; *Misawa*, 2004; *Vander Kaaden et al.*, 2015; *Warren et al.*, 1996]. The limited melt density range and overall low-melt density have important implications for the internal structure of Mercury's mantle and for the formation of primary and secondary crustal materials discussed below.

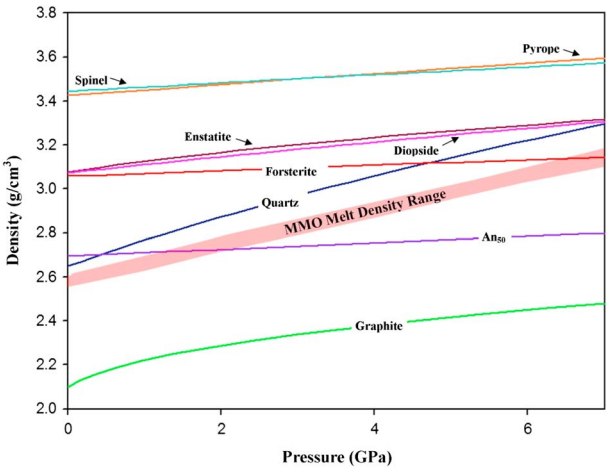


**Figure 4.** Comparison of the densities of possible Mercurian magma ocean melts to common rock-forming minerals, including graphite (green line), $An_{50}$ (purple line), quartz (blue line), forsterite (red line), diopside (pink line), enstatite (maroon line), pyrope (orange line), and spinel (turquoise line). All mineral density lines are derived from third-order Birch-Murnaghan equations of state at 1450°C. The density of the possible Mercurian magma ocean melt range refers to the melt region outlined in Figure 3.

### 6.2. How Easily Can Mercurian Melts Rise Through the Mantle?

In the Earth's mantle, there is a region where partial melts of the mantle are no longer buoyant with respect to surrounding mantle minerals due to the higher compressibility of silicate liquids as a function of pressure compared to most common mantle minerals. The depth at which this occurs is referred to as a density crossover. This depth within a planetary interior has important implications for the ability and likelihood of silicate melts to eventually erupting

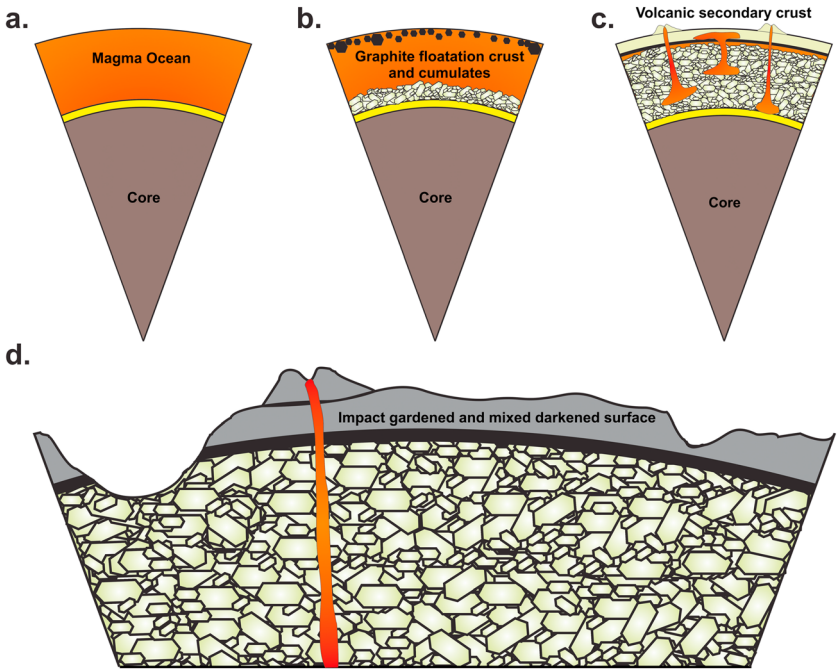


**Figure 5.** Cartoon illustrating the stages of a Mercurian magma ocean and subsequent primary and secondary crust formation. (a) Molten mantle (orange) and formation of the core (brown) and hypothesized FeS layer (yellow) at the base of the mantle. (b) Crystallization of the magma ocean continues with low-FeO cumulates sinking to the base of the mantle (light green) and the formation of a primary graphite floatation crust (black). (c) Continued crystallization followed by subsequent partial melting (orange) and volcanism to produce a secondary crust (light green). (d) Impacts to the planet have exposed portions of the mantle (green), as well as mixed the primary (black) and secondary crusts (dark gray), resulting in a darkened and spectrally neutral surface observed on Mercury today. The thickness of the graphite floatation crust is presently unknown, but it can be estimated as a function of the C abundance of the bulk silicate portion of Mercury (Figure 7). The thickness of the graphite floatation crust has been exaggerated for the purposes of this cartoon and does not appear in realistic proportions relative to the size of Mercury's core, mantle, and secondary crust.

onto the surface of the planet. To determine where these crossovers exist in the Mercurian mantle, we compared the range in melt density for Mercury (section 6.1) with the densities of many common rock-forming minerals that could be present within the Mercurian interior (Figure 4). Pertinent equations and parameters are given in section 4 and Table 2. Due to the low-expected FeO in Mercury's interior, Mg-rich end-members were chosen as they will be the least dense form of each mineral solid solution series. Upon examination of common rock-forming minerals, we found that there is a density crossover at ~6.8 GPa with our melt and $Fo_{100}$. Given the range of core-mantle boundary conditions from *Hauck et al.* [2013], however, this crossover should occur near the base of the mantle, or in the core of the planet, and would not inhibit the rise of any Mercurian magmas through the mantle. Furthermore, there is no density crossover between the NVP melt and Mg-rich pyroxenes, garnet, or spinel, which are all common minerals in other terrestrial planetary mantles [*Bertka and Fei*, 1997; *Neal*, 2001; *Ringwood*, 1966, 1975; *Smith et al.*, 1970; *Wood et al.*, 1970] and therefore candidate minerals for Mercury's mantle.

It is also possible that plagioclase and quartz are present in the Mercurian mantle [*Brown and Elkins-Tanton*, 2009], so they were also included among the minerals we investigated. There is a density crossover with the NVP melt and $An_{50}$ at ~1.9 GPa. Consequently, if this melt originated from deeper than ~1.9 GPa in a plagioclase-dominated source region, it would sink into the interior of Mercury. However, plagioclase is not stable at pressures greater than ~1 GPa [i.e., *Green and Hibberson*, 1970], so this density crossover would not inhibit the eruption of Mercurian melts. Additionally, Figure 4 shows that this Mercurian melt would be buoyant in a mantle consisting of quartz, since $SiO_2$ is consistently denser than the NVP melt. As a result of the locations of each density crossover, our data indicate that partial melts of the Mercurian mantle are buoyant in a mantle consisting of olivine, pyroxene, garnet, spinel, anorthite, and quartz in any proportions. This illustrates the extreme buoyancy conditions of Mercurian melts, and it indicates that partial melts of Mercury's mantle could rise and eventually erupt from depths as deep as the core-mantle boundary of the

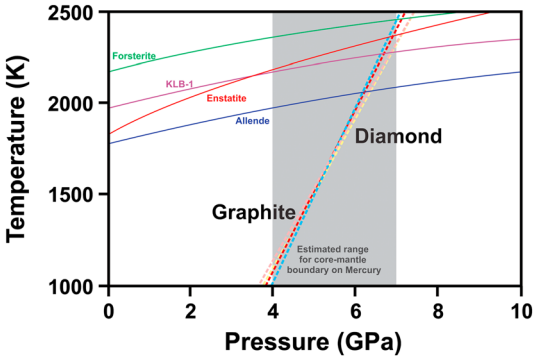


**Figure 6.** *P-T* phase diagram for carbon displaying the phase boundary between graphite and diamond, the pressure range of the Mercurian core-mantle boundary (gray regions taken, according to *Hauck et al.* [2013]), and liquidus curves for forsterite, terrestrial peridotite (KLB-1), enstatite, and a CV3 carbonaceous chondrite (Allende). The dashed lines represent various experimentally determined phase boundaries between graphite and diamond. The pink dashed line comes from *Clausing* [1997], the red dashed line comes from *Bundy et al.* [1961], the yellow dashed line is from *Kennedy and Kennedy* [1976], and the blue dashed line is from *Bundy et al.* [1996]. Data for each of the liquidus curves come from the following sources, forsterite (green) is from *Presnall and Walter* [1993], KLB-1 (purple) is from *Herzberg and Zhang* [1996], enstatite (red) is from *Boyd et al.* [1964], and Allende (dark blue) is from *Agee et al.* [1995].

planet. Furthermore, partial melts of the Mercurian interior would be less likely to stall during ascent, indicating Mercury may have erupted a greater percentage of its partial melts in comparison to other terrestrial planets, although other geophysical factors may have impeded magmatic eruptions on Mercury [e.g., *Byrne et al.*, 2014]. On Earth, the depth at which density crossovers occur for peridotite and mantle olivine is at much greater pressure (~10 GPa) [*Agee and Walker*, 1993] that is not reached in the Mercurian mantle. Importantly, Mercury represents the first terrestrial planet in our Solar System that does not contain regions within its mantle where partial melts would be more dense than the surrounding minerals, due to the compositionally distinct (low FeO) magmas coupled with the shallow depth of the Mercurian mantle.

### 6.3. Role of Graphite in Magmatic Evolution of Mercury

It has been suggested that Mercury differentiated through a magma ocean event in which substantial heating and melting of the planet took place [*Brown and Elkins-Tanton*, 2009; *Riner et al.*, 2009] (Figure 5a). On the Moon, we see evidence of a global lunar magma ocean through the presence of a primary anorthositic crust. According to existing lunar magma ocean crystallization models, plagioclase began to crystallize after about 75% crystallization [*Snyder et al.*, 1992] and was buoyant with respect to the FeO-rich residual melt, leading to plagioclase floatation and the formation of a primary anorthositic floatation crust [*Jolliff et al.*, 2000]. The low-FeO content and limited density range of Mercurian melts prohibit nearly all rock-forming minerals from forming a primary floatation crust on Mercury with the exception of graphite (Figures 3 and 4); therefore, it is the only candidate mineral that could have composed a primary floatation crust on Mercury.

The volatile-rich nature of Mercury's silicate portion, as determined by elevated K/Th and near chondritic K/Cl ratios [*Evans et al.*, 2014; *Peplowski et al.*, 2011, 2012a, 2014], lends support to the idea of volatile-rich phases in the Mercurian mantle. Consequently, Mercury may be enriched in carbon compared to other terrestrial planets [*Murchie et al.*, 2015; *Peplowski et al.*, 2015]. Elemental carbon phases, including diamond and graphite, occur in a wide variety of planetary materials from Earth, Moon, Mars, and asteroids [*Hirschmann and Withers*, 2008; *Shirey et al.*, 2013; *Steele et al.*, 2010; *Warren and Kallemeyn*, 1992], so it is not unreasonable to postulate the existence of elemental carbon on Mercury. The density difference between graphite and diamond in Mercury's interior, however, is of critical importance in the assessment of a possible floatation crust because only graphitic carbon would have a sufficiently low density to float in a Mercurian magma ocean. Mercury's shallow mantle results in a limited *P-T* profile that does not span into the diamond stability field (Figure 6). Graphite is therefore the stable phase of elemental carbon throughout the silicate portion of Mercury, which is a primary prerequisite to a graphite floatation crust. Elemental carbon has yet to be definitively detected on the Mercurian surface by the MESSENGER GRS [*Peplowski et al.*, 2015], and it is beyond the detection capabilities of MESSENGER's XRS. There is also absence of diagnostic spectral absorption features that suggest the presence of C in reflectance spectra. If primary elemental carbon is present on Mercury, then it will primarily be in the form of graphite and not diamond, although diamond could be present via formation by secondary processes such as impact or addition through late accretion.

The existence of graphite within the silicate portion of Mercury is dependent upon many factors, some of which are difficult to constrain. These include the initial C content of bulk Mercury, the distribution of C

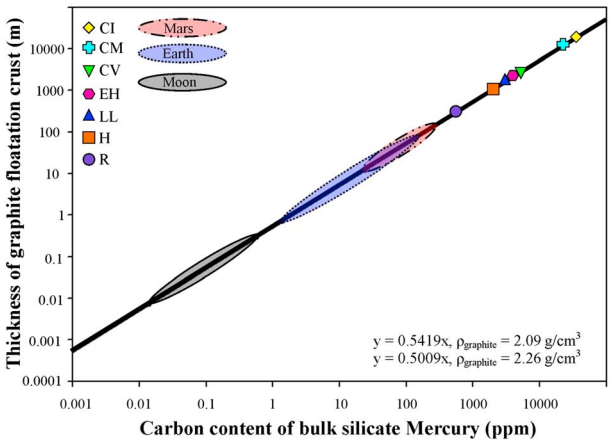


**Figure 7.** Thickness of possible graphite floatation crust (meters) as a function of carbon content (ppm) in the bulk silicate portion of Mercury. The model was computed using the parameters in Table 5 but assuming an average mantle density of 3.2 g/cm$^3$. The thickness of the line represents the range of graphite density (2.09 g/cm$^3$ to 2.26 g/cm$^3$) used in the calculation. Since the abundance of carbon in the bulk silicate portion of Mercury is unknown, the carbon content of various meteorites [*Lodders and Fegley*, 1998] and ranges for carbon in the silicate portions of the Moon [*McCubbin et al.*, 2015], the Earth [*Lodders and Fegley*, 1998], and Mars [*Hirschmann and Withers*, 2008] are plotted for comparison.

between Mercury's core and mantle, and whether or not Mercury's core was initially C saturated. Consequently, we look to both theoretical and empirical evidences to support or refute the idea of a primary floatation crust of graphite on Mercury. Although carbon likely represents one of the light elements incorporated into Mercury's core, metal-silicate partitioning studies of C at the specific *P-T-fO*$_2$ conditions of core formation on Mercury have not been determined. This remains the primary limiting factor to making estimates of the C abundances in the bulk silicate portion of Mercury. Regardless, at least some C would be incorporated into the silicate portion of Mercury as dissolved C–O, C–H, or carbonyl species or as a solid phase if the outer core and silicate liquid were C saturated [*Dasgupta*, 2013]. Carbon solubility in silicate melts is exceedingly low under highly reducing conditions [*Dasgupta et al.*, 2013], so graphite saturation would occur fairly early after the onset of magma ocean crystallization, and once formed, buoyancy forces would drive this graphite toward the surface of the magma ocean (Figure 5b). If Mercury's magma ocean had elevated hydrogen abundances, the magma ocean liquid would have a higher C solubility [*Ardia et al.*, 2013], which would delay the inevitable formation of graphite.

Assuming a graphite floatation crust formed on Mercury, the thickness and extent of that crust would be dictated by the amount of C allocated to the silicate portion of the planet and the efficiency of graphite floatation. Although we do not know how much carbon was originally in the mantle of Mercury, we can model the thickness of a graphite floatation crust as a function of the C abundance in the bulk silicate portion of the planet (Figure 7) using the parameters listed in Table 5 and the equations that follow. Assuming the entire inventory of carbon, C, in the silicate portion of Mercury floats to the surface due to buoyancy factors to produce a crust of homogeneous thickness over the entire surface of the planet, the thickness of that graphite floatation crust can be calculated by the following equation:

$$T = R - \left(R^3 - \frac{3}{4\pi}\frac{wt_C}{\rho_c}\right)^{\frac{1}{3}} \quad (5)$$

**Table 5.** Input Parameters Used to Calculate Thickness of Graphite Floatation Crust Using Equations (5)–(7)

| Parameter | Value | Reference |
|---|---|---|
| Radius of Mercury ($R$) | 2440 km | *Hauck et al.* [2013] |
| Radius of Mercury core ($R_c$) | 2020 km | *Hauck et al.* [2013] |
| Mantle density ($\rho_m$) (min) | 2800 kg/m$^3$ | *Hauck et al.* [2013] |
| Mantle density ($\rho_m$) (max) | 3600 kg/m$^3$ | *Hauck et al.* [2013] |
| Carbonaceous chondrite carbon abundance (C) (min) | 0.2 wt % | *Lodders and Fegley* [1998] |
| Carbonaceous chondrite carbon abundance (C) (max) | 3.45 wt % | *Lodders and Fegley* [1998] |
| Density of graphite ($\rho_c$) (min) | 2090 kg/m$^3$ | |
| Density of graphite ($\rho_c$) (max) | 2260 kg/m$^3$ | |

where $T$ is the thickness of a graphite floatation crust in meter, $R$ is the radius of Mercury in meter, $wt_C$ is the mass of carbon in the mantle in kilograms, and $\rho_c$ is the density of graphite in kg/m$^3$. Weight of carbon is defined as

$$wt_C = \rho_m V_m \left(\frac{C}{100}\right) \tag{6}$$

where $\rho_m$ is the density of the mantle in kg/m$^3$, $V_m$ is the volume of Mercury's mantle in cubic meter, and C is the weight percent of carbon in the mantle. $V_m$ is defined as

$$V_m = \frac{4}{3}\pi\left(R^3 - R_c^3\right) \tag{7}$$

where $R_c$ is the radius of Mercury's core in meter.

From this model, we have estimated the upper limit of the thickness of a graphite floatation crust using the abundances of C in carbonaceous chondrites, as Mercury is unlikely to have superchondritic abundances of C. *Lodders and Fegley* [1998] report a range of C abundances in carbonaceous chondrites with CI chondrites containing the most C (3.45 wt %) and CK chondrites containing the least C (0.22 wt %). Using these values, we have estimated that Mercury could have a primary floatation crust of graphite as thick as ~1–21 km if its bulk silicate had as much C as carbonaceous chondrites. However, even if Mercury had much less C, similar to the abundances estimated to be in the mantles of Earth or Mars, Mercury could still have had a primary graphite floatation crust that was 1–100 m in thickness (Figure 7). Once the carbon concentration in the bulk silicate portion of Mercury is better constrained, through future exploration and/or experimental studies, a more robust estimate of the thickness of this graphite floatation crust can be made using equations (5)–(7) and the results of this model depicted in Figure 7.

A primary graphite floatation crust on Mercury, albeit exotic, is supported by the dark color of Mercury's surface and the existence of low reflectance material covering at least 15% of its surface (>4 million km$^2$) [*Denevi et al.*, 2009]. If quartz and anorthite were primary components of Mercury's floatation crust [*Brown and Elkins-Tanton*, 2009], neither would produce a darkening effect. In fact, one would expect the surface of Mercury to approach the brightness of the lunar highlands with the addition of these two constituents, which is not consistent with MESSENGER data nor telescopic observations and analyses of the Mercurian surface. It has been suggested that this low reflectance material could be composed of opaque minerals, namely iron metal, iron-titanium oxides, graphite, and sulfides [*Denevi et al.*, 2009; *Robinson et al.*, 2008; *Xiao et al.*, 2013]. However, Fe-Ti oxides were ruled out as the source of the low reflectance material mainly due to the low abundance of Fe and Ti from MESSENGER XRS and GRS data [*Nittler et al.*, 2011; *Riner et al.*, 2010, 2011]. Furthermore, sulfides and iron metal have been largely ruled out as the darkening agent because both of these materials redden the UV-VIS spectrum while darkening, whereas the slope of UV-VIS spectra from Mercury is blue [*Blewett et al.*, 2013; *Murchie et al.*, 2015]. In contrast, nanophase Fe metal particles may not cause reddening and therefore cannot be ruled out as a darkening agent [*Lucey and Riner*, 2011]. By the process of elimination, *Murchie et al.* [2015] concluded that the low reflectance material on Mercury may be composed of coarse grained graphite, which would act as a darkening agent without reddening the slope. The source of this graphite, as well as the overall dark appearance of Mercury's surface, can be explained by a primary floatation crust on Mercury composed of graphite that was subsequently mixed with secondary materials by impact gardening (Figure 5d).

## 7. Conclusion

Following planetary differentiation and the formation of a primary crust on Mercury, partial melting in the mantle along with subsequent volcanism has resurfaced the majority of the planet (Figure 5c) [*Denevi et al.*, 2009, 2013; *Head et al.*, 2011]. Given the low and limited range of density of Mercurian melts (Figure 3), as well as the absence of density crossovers between these melts and possible mantle minerals (Figure 4), there are no restrictions on the depth of origin for these lavas. Therefore, eruptive volcanic products could have originated from as deep as the core-mantle boundary of Mercury. Additionally, partial melts of the Mercurian interior would be less likely to stall during ascent, indicating Mercury may have erupted a greater percentage of its partial melts in comparison to other terrestrial planets. Consequently, Mercury's extreme mantle composition and exceptionally shallow mantle may have led to exotic primary and secondary crust production, including a possible primary graphite floatation crust that was subsequently covered by secondary magmas derived from depths of melting as deep as the core-mantle boundary (Figure 5c). The primary crust, secondary

crust, and upper mantle have since been excavated and mixed by impact processes [*Rivera-Valentin and Barr*, 2014], as evidenced by the large number of craters observed on Mercury's surface [*Fassett et al.*, 2011], leading to the complex, chemically enigmatic, darkened surface that is observed today (Figure 5d).

**Acknowledgments**

All data used in this manuscript, including EPMA analyses, can be requested by contacting Kathleen Vander Kaaden (kvander@unm.edu). The authors would like to thank Whitney McCutcheon for assisting in FTIR analyses and Alison Santos for helpful discussions and assisting in multianvil runs. We also thank the MESSENGER Science Team for fruitful discussions regarding the interpretation of MESSENGER data. Additionally, the authors thank Nancy Chabot, Shoshana Weider, and an anonymous reviewer whose comments helped to substantially improve this manuscript. Steven Hauck, II (Editor) and Justin Filiberto (Associate Editor) are also thanked for their additional comments and for their editorial handling of this manuscript. This work was funded by a NASA Cosmochemistry grant NNX11AG76G to F.M.M. and New Mexico Space Grant Consortium Fellowship to K.E.V.K.

## References

Agee, C. B. (1998), Crystal-liquid density inversions in terrestrial and lunar magmas, *Phys. Earth Planet. Inter.*, *107*(1–3), 63–74.

Agee, C. B. (2008), Static compression of hydrous silicate melt and the effect of water on planetary differentiation, *Earth Planet. Sci. Lett.*, *265*(3–4), 641–654.

Agee, C. B., and D. Walker (1988), Static compression and olivine flotation in ultrabasic silicate liquid, *J. Geophys. Res.*, *93*(B4), 3437–3449, doi:10.1029/JB093iB04p03437.

Agee, C. B., and D. Walker (1993), Olivine Flotation in Mantle Melt, *Earth Planet. Sci. Lett.*, *114*(2–3), 315–324.

Agee, C. B., J. Li, M. C. Shannon, and S. Circone (1995), Pressure-temperature phase diagram for the Allende meteorite, *J. Geophys. Res.*, *100*(B9), 17,725–17,740, doi:10.1029/95JB00049.

Anderson, W. W., and T. J. Ahrens (1994), An equation of state for liquid iron and implications for the Earth's core, *J. Geophys. Res.*, *99*(B3), 4273–4284, doi:10.1029/93JB03158.

Angel, R. J. (2004), Equations of state of plagioclase feldspars, *Contrib. Mineral. Petrol.*, *146*(4), 506–512.

Ardia, P., M. M. Hirschmann, A. C. Withers, and B. D. Stanley (2013), Solubility of $CH_4$ in a synthetic basaltic melt, with applications to atmosphere-magma ocean-core partitioning of volatiles and to the evolution of the Martian atmosphere, *Geochim. Cosmochim. Acta*, *114*, 52–71.

Berger, J. A. (2012), Effect of halite and calcite coatings on thermal infrared spectra with implications for Mars exploration, MS thesis, Univ. of New Mexico.

Berthet, S., V. Malavergne, and K. Righter (2009), Melting of the Indarch meteorite (EH4 chondrite) at 1 GPa and variable oxygen fugacity: Implications for early planetary differentiation processes, *Geochim. Cosmochim. Acta*, *73*(20), 6402–6420.

Bertka, C. M., and Y. Fei (1997), Mineralogy of the Martian interior up to core-mantle boundary pressures, *J. Geophys. Res.*, *102*(B3), 5251–5264, doi:10.1029/96JB03270.

Birch, F. (1947), Finite elastic strain of cubic crystals, *Phys. Rev.*, *71*, 809–824.

Blewett, D. T., et al. (2013), Mercury's hollows: Constraints on formation and composition from analysis of geological setting and spectral reflectance, *J. Geophys. Res. Planets*, *118*, 1–20, doi:10.1029/2012JE004174.

Boyd, F. R., J. L. England, and B. T. C. Davis (1964), Effects of pressure on melting + polymorphism of enstatite $MgSiO_3$, *J. Geophys. Res.*, *69*(10), 2101–2109, doi:10.1029/JZ069i010p02101.

Brown, S. M., and L. T. Elkins-Tanton (2009), Compositions of Mercury's earliest crust from magma ocean models, *Earth Planet. Sci. Lett.*, *286*(3–4), 446–455.

Bundy, F. P., H. P. Bovenkerk, H. M. Strong, and R. H. Wentorf Jr. (1961), Diamond-graphite equilibrium line from growth and graphitization of diamond, *J. Chem. Phys.*, *35*(2), 383–391.

Bundy, F. P., W. A. Bassett, M. S. Weathers, R. J. Hemley, H. U. Mao, and A. F. Goncharov (1996), The pressure-temperature phase and transformation diagram for carbon; updated through 1994, *Carbon*, *34*(2), 141–153.

Burkemper, L. K., C. B. Agee, and K. A. Garcia (2012), Constraints on core formation from molybdenum solubility in silicate melts at high pressure, *Earth Planet. Sci. Lett.*, *335–336*(0), 95–104.

Byrne, P. K., C. Klimczak, A. M. C. Şengör, S. C. Solomon, T. R. Watters, and S. A. Hauck II (2014), Mercury's global contraction much greater than earlier estimates, *Nat. Geosci.*, *7*, 301–307.

Chabot, N. L., E. A. Wollack, R. L. Klima, and M. E. Minitti (2014), Experimental constraints on Mercury's core composition, *Earth Planet. Sci. Lett.*, *390*, 199–208.

Charlier, B., T. L. Grove, and M. T. Zuber (2013), Phase equilibria of ultramafic compositions on Mercury and the origin of the compositional dichotomy, *Earth Planet. Sci. Lett.*, *363*, 50–60.

Circone, S., and C. B. Agee (1996), Compressibility of molten high-Ti mare glass: Evidence for crystal-liquid density inversions in the lunar mantle, *Geochim. Cosmochim. Acta*, *60*(14), 2709–2720.

Clausing, R. (1997), Diamond morphology, in *Handbook of Industrial Diamonds and Diamond Films*, edited by M. Prelas et al., pp. 19–45, Kluwer Acad., New York.

Colonna, F., A. Fasolino, and E. J. Meijer (2011), High-pressure high-temperature equation of state of graphite from Monte Carlo simulations, *Carbon*, *49*, 364–368.

Conrad, P. G., C.-S. Zha, H.-K. Mao, and R. J. Hemley (1999), The high-pressure, single-crystal elasticity of pyrope, grossular, and andradite, *Am. Mineral.*, *84*(3), 374–383.

Dasgupta, R. (2013), Ingassing, storage, and outgassing of terrestrial carbon through geologic time, *Rev. Mineral. Geochem.*, *75*, 183–229.

Dasgupta, R., et al. (2013), Carbon solution and partitioning between metallic and silicate melts in a shallow magma ocean: Implications for the origin and distribution of terrestrial carbon, *Geochim. Cosmochim. Acta*, *102*, 191–212.

Denevi, B. W., et al. (2009), The evolution of Mercury's crust: A global perspective from MESSENGER, *Science*, *324*(5927), 613–618.

Denevi, B. W., et al. (2013), The distribution and origin of smooth plains on Mercury, *J. Geophys. Res. Planets*, *118*, 891–907, doi:10.1002/jgre.20075.

Dewaele, A., F. Datchi, and P. Loubeyre (2008), High pressure-high temperature equations of state of neon and diamond, *Phys. Rev. B*, *77*, 094106, doi:10.1103/PhysRevB.77.094106.

Dziewonski, A. M., and D. L. Anderson (1981), Preliminary reference Earth model, *Phys. Earth Planet. Inter.*, *25*(4), 297–256.

Evans, L. G., et al. (2012), Major-element abundances on the surface of Mercury: Results from the MESSENGER Gamma-Ray Spectrometer, *J. Geophys. Res.*, *117*, E00L07, doi:10.1029/2012JE004178.

Evans, L. G., P. N. Peplowski, D. S. Ebel, D. J. Lawrence, T. J. McCoy, L. R. Nittler, R. D. Starr, S. Z. Weider, and S. C. Solomon (2014), Chlorine on the surface of Mercury: Implications for Mercury's surface evolution, paper presented at 45th Lunar and Planetary Science Conference, The Woodlands, Tex.

Fassett, C. I., S. J. Kadish, J. W. Head, S. C. Solomon, and R. G. Strom (2011), The global population of large craters on Mercury and comparison with the Moon, *Geophys. Res. Lett.*, *38*, L10202, doi:10.1029/2011GL047294.

Fei, Y. (1995), Thermal expansion, in *Mineral Physics and Crystallography: A Handbook of Physical Constants*, edited by T. J. Ahrens, AGU Reference Shelf, Washington, D. C.

Fried, L. E., et al. (2002), EXP6: A new equation of state library for high pressure thermochemistry, paper presented at 12th International Symposium on Detonation, US Naval Research Office, San Diego, Calif.

Gessmann, C. K., B. J. Wood, D. C. Rubie, and M. R. Kilburn (2001), Solubility of silicon in liquid metal at high pressure: Implications for the composition of the Earth's core, *Earth Planet. Sci. Lett.*, *184*, 367–376.
Graham, E. K., J. A. Schwab, S. M. Sopkin, and H. Takei (1988), The pressure and temperature-dependence of the elastic properties of single-crystal fayalite $Fe_2SiO_4$, *Phys. Chem. Miner.*, *16*(2), 186–198.
Green, D. H., and W. Hibberson (1970), The instability of plagioclase in peridotite at high pressure, *Lithos*, *3*(3), 209–221.
Guo, X., et al. (2013), The density and compressibility of CaO-FeO-$SiO_2$ liquids at one bar: Evidence for four-coordinated $Fe^{2+}$ in the $CaFeO_2$ component, *Geochim. Cosmochim. Acta*, *120*, 206–219.
Guo, X., R. A. Lange, and Y. Ai (2014), Density and sound speed measurements on model basalt (An-Di-Hd) liquids at one bar: New constraints on the partial molar volume and compressibility of the FeO component, *Earth Planet. Sci. Lett.*, *388*, 283–292.
Hauck, S. A., II, et al. (2013), The curious case of Mercury's internal structure, *J. Geophys. Res. Planets*, *118*, 1204–1220.
Hazen, R. M. (1977), Effects of temperature and pressure on crystal-structure of ferromagnesian olivine, *Am. Mineral.*, *62*(3–4), 286–295.
Head, J. W., et al. (2011), Flood volcanism in the northern high latitudes of Mercury revealed by MESSENGER, *Science*, *333*(6051), 1853–1856.
Herzberg, C., and J. Z. Zhang (1996), Melting experiments on anhydrous peridotite KLB-1: Compositions of magmas in the upper mantle and transition zone, *J. Geophys. Res.*, *101*(B4), 8271–8295, doi:10.1029/96JB00170.
Hirschmann, M. M., and A. C. Withers (2008), Ventilation of $CO_2$ from a reduced mantle and consequences for the early Martian greenhouse, *Earth Planet. Sci. Lett.*, *270*(1–2), 147–155.
Hugh-Jones, D. (1997), Thermal expansion of $MgSiO_3$ and $FeSiO_3$ ortho- and clinopyroxenes, *Am. Mineral.*, *82*(7–8), 689–696.
HughJones, D. A., and R. J. Angel (1994), A compressional study of $MgSiO_3$ orthoenstatite up to 8.5-GPa, *Am. Mineral.*, *79*(5–6), 405–410.
Isaak, D. G., E. K. Graham, J. D. Bass, and H. Wang (1993), The elastic properties of single-crystal fayalite as determined by dynamical measurement techniques, *Pure Appl. Geophys.*, *141*(2–4), 393–414.
Jacobs, M. H. G., and B. de Jong (2007), Placing constraints on phase equilibria and thermophysical properties in the system MgO-$SiO_2$ by a thermodynamically consistent vibrational method, *Geochim. Cosmochim. Acta*, *71*(14), 3630–3655.
Javoy, M., et al. (2010), The chemical composition of the Earth: Enstatite chondrite models, *Earth Planet. Sci. Lett.*, *293*, 259–268.
Jolliff, B. L., J. J. Gillis, L. A. Haskin, R. L. Korotev, and M. A. Wieczorek (2000), Major lunar crustal terranes: Surface expressions and crust-mantle origins, *J. Geophys. Res.*, *105*(E2), 4197-4216, doi:10.1029/1999JE001103.
Kennedy, C. S., and G. C. Kennedy (1976), Equilibrium boundary between graphite and diamond, *J. Geophys. Res.*, *81*(14), 2467–2470, doi:10.1029/JB081i014p02467.
Knoche, R., and R. W. Luth (1996), Density measurements on melts at high pressure using the sink/float method: Limitations and possibilities, *Chem. Geol.*, *128*(1–4), 229–243.
Lange, R. A., and I. S. E. Carmichael (1987), Densities of $Na_2O$-$K_2O$-CaO-MgO-FeO-$Fe_2O_3$-$Al_2O_3$-$TiO_2$-$SiO_2$ liquids: New measurements and derived partial molar properties, *Geochim. Cosmochim. Acta*, *51*(11), 2931–2946.
Li, J., and C. B. Agee (2001), Element partitioning constraints on the light element composition of the Earth's core, *Geophys. Res. Lett.*, *28*(1), 81–81, doi:10.1029/2000GL012114.
Liu, Q., and R. A. Lange (2001), The partial molar volume and thermal expansivity of $TiO_2$, in alkali silicate melts: Systematic variation with Ti coordination, *Geochim. Cosmochim. Acta*, *65*(14), 2379–2393.
Liu, W., and B. Li (2006), Thermal equation of state of $(Mg_{0.9}Fe_{0.1})_2SiO_4$ olivine, *Phys. Earth Planet. Inter.*, *157*, 188–195.
Lodders, K., and B. Fegley (1998), *The Planetary Scientist's Companion*, Oxford Univ. Press, New York.
Lucey, P. G., and M. A. Riner (2011), The optical effects of small iron particles that darken but do not redden: Evidence of intense space weathering on Mercury, *Icarus*, *212*(2), 451–462.
Malavergne, V., M. J. Toplis, S. Berthet, and J. Jones (2010), Highly reducing conditions during core formation on Mercury: Implications for internal structure and the origin of a magnetic field, *Icarus*, *206*(1), 199–209.
Mandeville, C. W., et al. (2002), Determination of molar absorptivities for infrared absorption bands of H2O in andesitic glasses, *Am. Mineral.*, *87*(7), 813–821.
McCubbin, F. M., H. Nekvasil, A. D. Harrington, S. M. Elardo, and D. H. Lindsley (2008), Compositional diversity and stratification of the Martian crust: Inferences from crystallization experiments on the picrobasalt Humphrey from Gusev Crater, Mars., *J. Geophys. Res.*, *113*, E11013, doi:10.1029/2008JE003165.
McCubbin, F. M., M. A. Riner, K. E. Vander Kaaden, and L. K. Burkemper (2012), Is Mercury a volatile-rich planet?, *Geophys. Res. Lett.*, *39*, L09202, doi:10.1029/2012GL051711.
McCubbin, F. M., et al. (2015), Magmatic volatiles (H, C, N, F, S, Cl) in the lunar mantle, crust, and regolith: Abundances, distributions, processes, and reservoirs, *Am. Mineral.*, *100*, in press.
Misawa, K. (2004), The Yamato 980459 olivine-phyric shergottite consortium, *Antarct. Meteroite Res.*, *17*, 1–12.
Murchie, S. L., et al. (2015), Orbital multispectral mapping of Mercury using the MESSENGER Mercury Dual Imaging System: Evidence for the origins of plains units and low-reflectance material, *Icarus*.
Neal, C. R. (2001), Interior of the Moon: The presence of garnet in the primitive deep lunar mantle, *J. Geophys. Res.*, *106*(E11), 27,865–827,885, doi:10.1029/2000JE001386.
Nishida, K., E. Ohtani, S. Urakawa, A. Suzuki, T. Sakamaki, H. N. Terasaki, and Y. N. Katayama (2011), Density measurement of liquid FeS at high pressures using synchrotron X-ray absorption, *Am. Mineral.*, *96*, 864–868.
Nittler, L. R., et al. (2011), The major-element composition of Mercury's surface from MESSENGER X-ray spectrometry, *Science*, *333*(6051), 1847–1850.
Ochs, F. A., and R. A. Lange (1999), The density of hydrous magmatic liquids, *Science*, *283*(5406), 1314–1317.
Peplowski, P. N., et al. (2011), Radioactive elements on Mercury's surface from MESSENGER: Implications for the planet's formation and evolution, *Science*, *333*(6051), 1850–1852.
Peplowski, P. N., et al. (2012a), Variations in the abundances of potassium and thorium on the surface of Mercury: Results from the MESSENGER Gamma-Ray Spectrometer, *J. Geophys. Res.*, *117*, E00L04, doi:10.1029/2012JE004141.
Peplowski, P. N., E. A. Rhodes, D. K. Hamara, D. J. Lawrence, L. G. Evans, L. R. Nittler, and S. C. Solomon (2012b), Aluminum abundance on the surface of Mercury: Applications of a new background-reduction technique for the analysis of gamma-ray spectroscopy data, *J. Geophys. Res.*, *117*, E00L10, doi:10.1029/2012JE004181.
Peplowski, P. N., et al. (2014), Enhanced sodium abundance in Mercury's north polar region revealed by the MESSENGER Gamma-Ray Spectrometer, *Icarus*, *228*, 86–95.
Peplowski, P. N., et al. (2015), Constraints on the abundance of carbon in near-surface materials on Mercury: Results from the MESSENGER Gamma-Ray Spectrometer, *Planet. Space Sci.*, doi:10.1016/j.pss.2015.01.008.
Presnall, D. C., and M. J. Walter (1993), Melting of forsterite, $Mg_2SiO_4$, from 9.7 to 16.5 GPa, *J. Geophys. Res.*, *98*(B11), 19,777–19,783, doi:10.1029/93JB01007.

Ramsey, W. H., and P. M. S. Blackett (1948), On the constitution of the terrestrial planets, *Mon. Not. R. Astron. Soc.*, *108*(5), 406–413.
Ricolleau, A., Y. Fei, A. Corgne, J. Siebert, and J. Badro (2011), Oxygen and silicon contents of Earth's core from high pressure metal-silicate partitioning experiments, *Earth Planet. Sci. Lett.*, *310*(3–4), 409–421.
Riner, M. A., P. G. Lucey, S. J. Desch, and F. M. McCubbin (2009), Nature of opaque components on Mercury: Insights into a Mercurian magma ocean, *Geophys. Res. Lett.*, *36*, L02201, doi:10.1029/2008GL036128.
Riner, M. A., F. M. McCubbin, P. G. Lucey, G. J. Talyor, and J. J. Gillis-Davis (2010), Mercury surface composition: Integrating petrologic modeling and remote sensing data to place constraints on FeO abundance, *Icarus*, *209*(2), 301–313.
Riner, M. A., P. G. Lucey, F. M. McCubbin, and G. J. Taylor (2011), Constraints on Mercury's surface composition from MESSENGER neutron spectrometer data, *Earth Planet. Sci. Lett.*, *308*(1–2), 107–114.
Ringwood, A. E. (1966), Chemical evolution of the terrestrial planets, *Geochim. Cosmochim. Acta*, *30*, 41–104.
Ringwood, A. E. (1975), *Composition and Petrology of the Earth's Mantle*, 618 pp., McGraw-Hill, New York.
Rivera-Valentin, E. G., and A. C. Barr (2014), Impact-induced compositional variations on Mercury, *Earth Planet. Sci. Lett.*, *391*, 234–242.
Robinson, M. S., et al. (2008), Reflectance and color variations on Mercury: Regolith processes and compositional heterogeneity, *Science*, *321*(5885), 66–69.
Schutt, D. L., and C. E. Lesher (2006), Effects of melt depletion on the density and seismic velocity of garnet and spinel lherzolite, *J. Geophys. Res.*, *11*, B05401, doi: 10.1029/2003JB002950.
Shirey, S. B., P. Cartigny, D. J. Frost, S. Keshav, F. Nestola, P. Nimis, D. G. Pearson, N. V. Sobolev, and M. J. Walter (2013), Diamonds and the geology of mantle carbon, *Rev. Mineral. Geochem.*, *75*, 355–421.
Skinner, B. J. (1966), Thermal expansion, in *Handbook of Physical Constants*, *Revised Edition*, vol. 97, edited by J. S. P. Clark, pp. 75–96, Geol. Soc. Am. Mem., doi:10.1130/MEM97-p75.
Smith, D. E., et al. (2012), Gravity field and internal structure of Mercury from MESSENGER, *Science*, *336*, 214–217.
Smith, J. R., and C. B. Agee (1997), Compressibility of molten "green glass" and crystal-liquid density crossovers in low-Ti lunar magma, *Geochim. Cosmochim. Acta*, *61*(10), 2139–2145.
Smith, J. V., A. T. Anderson, R. C. Newton, E. J. Olsen, and P. J. Wyllie (1970), A petrologic model for the Moon based on petrogenesis, experimental petrology, and physical properties, *J. Geol.*, *78*(4), 381–405.
Smyth, J. R. (1975), High-temperature crystal-chemistry of fayalite, *Am. Mineral.*, *60*(11–1), 1092–1097.
Snyder, G. A., L. A. Taylor, and C. R. Neal (1992), A chemical-model for generating the sources of mare basalts—Combined equilibrium and fractional crystallization of the lunar magmasphere, *Geochim. Cosmochim. Acta*, *56*(10), 3809–3823.
Solomon, S. C., et al. (2001), The MESSENGER mission to Mercury: Scientific objectives and implementation, *Planet. Space Sci.*, *49*, 1445–1465.
Steele, A., F. M. McCubbin, M. Fries, M. Glamoclija, L. Kater, and H. Nekvasil (2010), Graphite in an Apollo 17 impact melt breccia, *Science*, *329*(5987), 51–51.
Sumino, Y., and O. L. Anderson (1984), Elastic constants of minerals, in *CRC Handbook of the Physical Properties of Rocks*, edited by S. Carmichael, CRC Press, Boca Raton, Fla.
Suzuki, A., E. Ohtani, and T. Kato (1998), Density and thermal expansion of a peridotite melt at high pressure, *Phys. Earth Planet. Inter.*, *107*(1–3), 53–61.
Suzuki, I. (1975), Thermal expansion of periclase and olivine, and their anharmonic properties, *J. Phys. Earth*, *23*, 145–159.
Suzuki, I., K. Seya, H. Takei, and Y. Sumino (1981), Thermal expansion of fayalite, $Fe_2SiO_4$, *Phys. Chem. Miner.*, *7*(2), 60–63.
Tsuno, K., D. J. Frost, and D. C. Rubie (2013), Simultaneous partitioning of silicon and oxygen into the Earth's core during early Earth differentiation, *Geophys. Res. Lett.*, *40*, 66–71, doi:10.1029/2012GL054116.
van Kan Parker, M., C. B. Agee, M. S. Duncan, and W. van Westrenen (2011), Compressibility of molten Apollo 17 orange glass and implications for density crossovers in the lunar mantle, *Geochim. Cosmochim. Acta*, *75*(4), 1161–1172.
Vander Kaaden, K. E., C. B. Agee, and F. M. McCubbin (2015), Density and compressibility of the molten lunar picritic glasses: Implications for the roles of Ti and Fe in the structures of silicate melts, *Geochim. Cosmochim. Acta*, *149*, 1–20.
Warren, P. H., and G. W. Kallemeyn (1992), Explosive volcanism and the graphite-oxygen fugacity buffer on the parent asteroid(s) of the urelite meteorites, *Icarus*, *100*, 110–126.
Warren, P. H., et al. (1996), Compositional-petrologic investigations of eucrites and the QUE94201 shergottite, paper presented at Proc. NIPR Sym. Antarctic Meteorites, Nat. Inst. Polar Res., Tokyo.
Weider, S. Z., L. R. Nittler, R. D. Starr, T. J. McCoy, K. R. Stockstill-Cahill, P. K. Byrne, B. W. Denevi, J. W. Head, and S. C. Solomon (2012), Chemical heterogeneity on Mercury's surface revealed by the MESSENGER X-ray spectrometer, *J. Geophys. Res.*, *117*, E00L05, doi:10.1029/2012JE004153.
Weider, S. Z., L. R. Nittler, R. D. Starr, E. J. Crapster-Pregont, and S. C. Solomon (2014a), Geochemical terranes on the innermost planet: Possible origins of Mercury's high-magnesium region, paper presented at 45th Lunar and Planetary Science Conference, The Woodlands, Tex.
Weider, S. Z., L. R. Nittler, R. D. Starr, T. J. McCoy, and S. C. Solomon (2014b), Variations in the abundance of iron on Mercury's surface from MESSENGER X-Ray Spectrometer observations, *Icarus*, *235*, 170–186.
Weider, S. Z., et al. (2015), Evidence for geochemical terranes on Mercury: The first global mapping of major elements on the surface of the innermost planet, *Earth Planet. Sci. Lett.*
Wood, J. A., J. S. Dickey, U. B. Marvin, and B. N. Powell (1970), Lunar anorthosites and a geophysical model of the Moon, *Proceedings of the Apollo 11 Lunar Science Conference*, *1*, 965-988.
Xiao, Z., R. G. Strom, D. T. Blewett, P. K. Byrne, S. C. Solomon, S. L. Murchie, A. L. Sprague, D. L. Domingue, and J. Helbert (2013), Dark spots on Mercury: A distinctive low-reflectance material and its relation to hollows, *J. Geophys. Res. Planets*, *118*, 1–14.
Zhang, L., H. Ahsbahs, A. Kutoglu, and C. A. Geiger (1999), Single-crystal hydrostatic compression of synthetic pyrope, almandine, spessartine, grossular and andradite garnets at high pressures, *Phys. Chem. Miner.*, *27*(1), 52–58.
Zolotov, M. Y., A. L. Sprague, S. A. Hauck II, L. R. Nittler, S. C. Solomon, and S. Z. Weider (2013), The redox state, FeO content, and origin of sulfur-rich magmas on Mercury, *J. Geophys. Res. Planets*, *118*, doi:10.1029/2012JE004274.